

# The Human Interferon Receptor: NMR-Based Modeling, Mapping of the IFN- $\alpha$ 2 Binding Site, and Observed Ligand-Induced Tightening<sup>†,‡</sup>

Jordan H. Chill,<sup>§</sup> Rachel Nivasch,<sup>§</sup> Rina Levy,<sup>§</sup> Shira Albeck,<sup>||</sup> Gideon Schreiber,<sup>||</sup> and Jacob Anglister<sup>\*,§</sup>

*Departments of Structural Biology and Biological Chemistry, The Weizmann Institute of Science, Rehovot 76100, Israel*

*Received September 10, 2001*

**ABSTRACT:** The human interferon receptor (IFNAR) mediates the antiviral and antiproliferative activities of type I interferons (IFNs). This receptor is comprised of subunits IFNAR1 and IFNAR2, the latter exhibiting nanomolar affinity for IFNs. Here the extracellular domain of IFNAR2 (IFNAR2-EC), a soluble 25 kDa IFN-binding polypeptide, and its complex with IFN- $\alpha$ 2 were studied using multidimensional NMR. IFNAR2-EC is comprised of two fibronectin-III (FN-III) domains connected by a helical hinge region. The deduced global fold was utilized to improve the alignment of IFNAR2-EC against structurally related receptors and to model its structure. A striking feature of IFNAR2-EC is the limited and localized deviations in chemical shifts exhibited upon ligand binding, observed for only 15% of its backbone <sup>1</sup>H and <sup>15</sup>N nuclei. Analysis of these deviations maps the IFN- $\alpha$ 2 binding site upon IFNAR2-EC to a contiguous surface on the N-terminal domain, including the S3–S4 loop (residues 44–53), the S5–S6 loop and S6  $\beta$ -strand (residues 74–82), and the S7  $\beta$ -strand and the hinge region (residues 95–105). The C-terminal domain contributes only marginally to ligand binding, and no change in the hypothesized interdomain interface is observed. The proposed binding domain encompasses all residues implicated by mutagenesis studies in IFN binding, and suggests adjacent residues cooperate in forming the binding surface. D<sub>2</sub>O-exchange experiments indicate that binding of IFN- $\alpha$ 2 induces tightening of the N-terminal domain of IFNAR2-EC. This increase in receptor rigidity may play an important role in initiating the intracellular stage of the IFN signaling cascade.

Type I interferons are a family of homologous helical cytokines secreted by lymphocytes and fibroblasts in response to viral infection and cancer. They provide an early line of antiviral defense and are essential for the survival of higher vertebrates (1, 2). IFNs<sup>1</sup> also have several important pharmaceutical applications, notably, in cancer therapy and treatment of certain viral diseases. In humans, this family of cytokines consists of 12 different IFN- $\alpha$  species, one IFN- $\beta$ , one IFN- $\tau$ , and one IFN- $\omega$ . Members of this family exhibit significant sequence homology, with an ~80% level of

identity observed between IFN- $\alpha$  isotypes and a 50% level of identity between IFN- $\beta$  and a consensus IFN- $\alpha$  sequence (3, 4). Type I IFNs share a common cell-surface receptor in humans, consisting of two subunits, IFNAR1 (5) and IFNAR2 (6), which associate upon IFN binding (7). The association of IFNAR2 and IFNAR1 effected by IFN binding triggers a cascade of events, which activates a multitude of proteins that inhibit viral replication and cell growth and control apoptosis (2). IFNAR2 alone can bind both IFN- $\alpha$  and IFN- $\beta$  subtypes, and is the major ligand-binding component of the receptor complex, exhibiting a high affinity ( $K_D \sim 3$  nM) for IFN- $\alpha$ 2. This affinity is increased up to 20-fold upon formation of the ternary complex, which includes IFNAR1. The intrinsic affinity of IFNAR1 for IFN- $\alpha$ 2 is low ( $K_D > 100$  nM) (7).

The ability of IFN- $\alpha$  and IFN- $\beta$  to elicit different cellular responses (8) upon binding to what appears to be a single receptor is of particular interest (9). Mutational studies monitoring IFN-induced activity suggest that IFNAR2 is responsible for their differential recognition (10–12). The functional role of IFNAR1 in this context has been difficult to substantiate due to the absence of human cells that constitutively fail to express IFNAR1. A recent mutational analysis of IFN- $\beta$  suggests the existence of binding sites for IFNAR1 and IFNAR2 on opposite faces of the IFN molecule, but results pertaining to the postulated IFNAR1 binding site were less conclusive (13).

While previously determined three-dimensional structures of human IFNs include IFN- $\alpha$ 2a (14), IFN- $\alpha$ 2b (15), and

<sup>†</sup> This study was supported by NIH Grant GM53329 and by the Israel Academy of Science (J.A.). J.A. is the Dr. Joseph and Ruth Owades Professor of Chemistry.

<sup>‡</sup> The chemical shifts have been deposited in BioMagResBank under accession number 5049.

<sup>\*</sup> To whom correspondence should be addressed. Telephone: 972-8-9343394. Fax: 972-8-9344136. E-mail: jacob.anglister@weizmann.ac.il.

<sup>§</sup> Department of Structural Biology.

<sup>||</sup> Department of Biological Chemistry.

<sup>1</sup> Abbreviations: FN-III, fibronectin-III module; FPLC, fast performance liquid chromatography; GHR, growth hormone receptor; hCRI and -II, helical cytokine class I and II receptors, respectively; HSQC, heteronuclear single-quantum coherence; IFN, interferon; IFNAR2, subunit 2 of the IFN- $\alpha$  receptor; IFNAR2-EC, extracellular domain of IFNAR2; IFN $\gamma$ R, IFN- $\gamma$  receptor; IL-4R, interleukin-4 receptor; NOE, nuclear Overhauser effect; NOESY, NOE spectroscopy; NMR, nuclear magnetic resonance; QSFF, Q-Sepharose fast flow; TFR, tissue factor receptor; TROSY, transverse relaxation optimized spectroscopy. Numbering of residues begins with the SYDSP sequence at the N-terminus of IFNAR2-EC.  $\beta$ -Strands are termed S1–S7 for the N-terminal subdomain and S8–S14 for the C-terminal subdomain, and loops are identified by their flanking  $\beta$ -strands.

IFN- $\beta$  (16, 17), no structure has been proposed for either receptor component. Sequence alignment suggests both IFNAR1 and IFNAR2 belong to the family of helical cytokine class II receptors (hCR2) (18). On the basis of sequence homology with receptors of this family with known structures, such as the IFN- $\gamma$  receptor (IFN $\gamma$ R) (19) and the tissue factor receptor (TFR) (20), the extracellular N-terminus of IFNAR2 has been postulated to consist of two immunoglobulin fold subdomains of the FN-III type, each comprised of seven  $\beta$ -strands divided into two  $\beta$ -sheets (21). Structural study of IFNAR2 and its binding of IFN ligands has recently become feasible, as Schreiber and co-workers successfully expressed and purified the extracellular domain of IFNAR2 (IFNAR2-EC). IFNAR2-EC is a soluble 25 kDa polypeptide that retains full binding activity of IFNAR2 and competitively inhibits the cellular antiviral activity of IFN- $\alpha$ 2 (22). The binding site for IFN ligands upon cellular IFNAR2, as well as specific residues involved in binding, has been established by site-directed mutagenesis (10) and immunoblocking studies (12). Studies conducted with both intact IFNAR2 and IFNAR2-EC suggest partially overlapping binding sites for IFN- $\alpha$  and IFN- $\beta$  subtypes but different contributions of specific residues to the exhibited affinity.

The structure of IFNAR2-EC was modeled on the basis of its homology to TFR (21% sequence identity) and IFN $\gamma$ R (17% sequence identity). In this model, all residues implicated in IFN- $\alpha$ 2 binding are located on a contiguous surface formed by two protruding loops of the N-terminal immunoglobulin domain and the segment connecting the two domains (11). The C-terminal domain does not contribute significantly to IFN- $\alpha$ 2 binding. Homology modeling of the IFNAR2-IFN- $\alpha$ 8 complex according to the known structure of the growth hormone (GH) in complex with its class I receptor (12% sequence identity between the receptor extracellular domains) postulates a binding site comprised by segments of residues 43–50, 70–78, 100–110, 130–137, and 189–194 of IFNAR2 (23). This proposed binding site is in agreement with the results of an alanine scanning mutagenesis study performed on TFR (24).

A detailed structural analysis of IFNAR2-EC and its complexes with type I IFNs could greatly enhance our molecular understanding of IFN binding and signaling in this intriguing system. This is especially true in light of the limitations that the low level of sequence identity between IFNAR2-EC and related receptors places upon attempts to model its structure. In this study, we map the IFN- $\alpha$ 2 binding site and determine global changes in IFNAR2-EC conformation upon ligand binding. A new model for IFNAR2-EC has been calculated using the secondary structure and the global fold deduced from a multidimensional NMR study of IFNAR2-EC and its complex with IFN- $\alpha$ 2. Deuterium-exchange experiments show that IFN binding induces considerable tightening of the structure of the IFNAR2-EC N-terminal domain. The implications of our results are discussed in the context of previously reported structural and biological aspects of IFN binding to IFNAR2.

## MATERIALS AND METHODS

**Protein Expression and Purification.** The pTZT7U18 plasmid containing the gene encoding the IFNAR2-EC polypeptide and protocols for heterologous overexpression

of unlabeled IFNAR2-EC have been previously described (22). Uniformly  $^{15}\text{N}$ -labeled and  $^{13}\text{C}$ ,  $^{15}\text{N}$ -doubly labeled IFNAR2-EC were overexpressed using appropriately labeled Celtone medium (Martek Biosciences) supplemented with 0.375% glycerol ( $^{13}\text{C}$ -labeled for the doubly labeled polypeptide), RPMI 1640 vitamin cocktail (Gibco), 1 mM  $\text{MgSO}_4$ , 50 mM  $\text{KH}_2\text{PO}_4$ , and 50 mM  $\text{K}_2\text{HPO}_4$ . Optimal yields were obtained using 50 mL cultures in 1 L flasks grown at 37 °C. IFNAR2-EC expression was induced by 0.5 mM isopropyl  $\beta$ -D-thiogalactopyranoside and 1:1000 (v/v) M13 phage. Cells were harvested after 3–4 h. For expression of 50%  $^2\text{H}$ -,  $^{13}\text{C}$ ,  $^{15}\text{N}$ -labeled IFNAR2-EC, cells were adapted to the deuterated environment through multiple steps with progressively higher percentages of  $\text{D}_2\text{O}$  and deuteration in nutrients, and cells were harvested 10–16 h after induction. Cells were lysed using lysosyme, followed by a freeze–thaw cycle and sonication, and inclusion bodies were washed and resonicated using a urea-containing buffer. The inclusion bodies were then dissolved in excessive amounts of 9 M urea at pH 8.4, maintaining an  $\text{OD}_{280}$  of  $<0.5$  to ensure efficient refolding. IFNAR2-EC was refolded by double dialysis against Tris buffer at pH 8.4. Refolded IFNAR2-EC was purified to  $>98\%$  homogeneity on an AKTA FPLC system using the HiTrap QSFF anion-exchange and Superdex 75 HR 10/30 size-exclusion columns (all from Pharmacia). The protein was concentrated by centrifugation in Vivaspin tubes (Vivasciences, molecular mass cutoff of 10 kDa), and desalination effected by repeated dilutions with an appropriate buffer. Activity of IFNAR2-EC was assayed prior to sample preparation by incubation with IFN- $\alpha$ 2 for 10 min at ambient temperature and detection of the 43 kDa IFNAR2-EC–IFN- $\alpha$ 2 complex using size-exclusion chromatography. This protocol produced 4–8 mg of IFNAR2-EC per liter of Celtone medium.

**Preparation and Purification of the IFNAR2-EC–IFN- $\alpha$ 2 Complex.** IFN- $\alpha$ 2 was expressed in milligram quantities as described elsewhere (22) and purified using the HiTrap QSFF anion-exchange and Superdex 75 HR 10/30 size-exclusion columns (both from Pharmacia) with Tris buffer at pH 8.4 followed by RP-HPLC using an acetonitrile gradient. IFNAR2-EC (at 1–1.5  $\mu\text{M}$ ) and IFN- $\alpha$ 2 (in 10% excess) were incubated in 25 mM Tris buffer (pH 8.2) containing 0.02%  $\text{NaN}_3$  for 1–2 h at ambient temperature. After being concentrated 10-fold, the IFNAR2-EC–IFN- $\alpha$ 2 complex was purified using a preparative Superdex 75 size-exclusion column (Pharmacia), with 250 mM  $\text{NaCl}$  and 0.02%  $\text{NaN}_3$  in 25 mM Tris (pH 8) as the running buffer. The complex elutes at a volume corresponding to a 43 kDa protein, confirming its 1:1 stoichiometry.

**Optimization of Measurement Conditions and Sample Preparation.** Samples used for NMR measurements included uniformly  $^{15}\text{N}$ - and  $^{13}\text{C}$ -labeled IFNAR2-EC and 50%- $^2\text{H}$ -, 98%- $^{15}\text{N}$ ,  $^{13}\text{C}$ -labeled IFNAR2-EC both in the free form and in complex with unlabeled IFN- $\alpha$ 2. A combinatorial array of 0.5 mM IFNAR2-EC microsamples in 25 mM Tris buffer (containing 0.02%  $\text{NaN}_3$  as a bactericide) at 37 °C was designed to determine the optimal measurement conditions for this polypeptide. Variables that were studied were pH (7.0–8.0),  $\text{NaCl}$  concentration (0–200 mM), and the stabilizing effects of the organic cosolvents DMSO and ethanolamine and the chaotropic additive CHAPS. IFNAR2-EC stability was monitored by the ratio of active monomeric to

aggregated protein as seen in a size-exclusion chromatogram. Optimal conditions used for preparation of NMR samples were a 95% H<sub>2</sub>O/5% D<sub>2</sub>O mixture and 25 mM Tris buffer (pH 8.0) (98% deuterated if necessary) containing 0.02% NaN<sub>3</sub> as a bactericide, with the NaCl concentration kept below 1 mM. Desalination was effected by repeated dilution with 25 mM Tris (pH 8) and 0.02% NaN<sub>3</sub> buffer and concentration in Fugisep tubes (Intersep, molecular mass cutoff of 10 kDa). Samples in D<sub>2</sub>O were similarly prepared by repeated dilution and concentration using 99.9% D<sub>2</sub>O and perdeuterated (98% deuterated) Tris buffer. All samples were concentrated to volumes of 300–350  $\mu$ L (final IFNAR2-EC concentration of 0.3–0.5 mM). IFNAR2-EC samples were stable under these conditions and at 35 °C for a period of 2–3 months, with negligible aggregation or denaturation. The IFNAR2-EC–IFN- $\alpha$ 2 complex was stable under these conditions at 40 °C for more than 30 days. Amide proton  $T_2$  relaxation times for free IFNAR2-EC under these conditions were 13–16 ms, typical values for a monomeric 25 kDa protein. Amide proton  $T_2$  values for the IFNAR2-EC–IFN- $\alpha$ 2 complex under these conditions were 8–9 and 9.5–11 ms at 35 and 40 °C, respectively, typical values for a 43 kDa polypeptide.

**NMR Measurements for Free IFNAR2-EC.** All NMR spectra for free <sup>13</sup>C- and <sup>15</sup>N-labeled IFNAR2-EC were acquired at 35 °C on Bruker DRX 800 MHz and DMX 600 MHz spectrometers equipped with a  $z$ -gradient triple-resonance probe (Bruker). Data were processed and analyzed on an Octane workstation (Silicon Graphics) using XWIN-NMR and AURELIA (25) and NMRPipe (26). Measurements of amide proton  $T_2$  relaxation times utilized a 1,1 echo sequence. For the two-dimensional (2D) [<sup>1</sup>H,<sup>15</sup>N]HSQC experiment, 256  $t_1$  increments at a sweep width of 1946 Hz and 350  $t_2$  points at a sweep width of 9600 Hz were acquired. The following experiments were carried out for free IFNAR2-EC (on the 800 MHz spectrometer unless otherwise stated): three-dimensional (3D) HNCO and 3D HNCA (27, 28), 3D CBCA(CO)NH on the DMX 600 MHz spectrometer (29), 3D HNCACB (30), 3D (H)-C-(CCO)NH TOCSY on the DMX 600 MHz spectrometer (31), and 3D HBHA-(CBCACO)NH (32). Experiments used to derive NOESY connectivities and internuclear distances were 3D <sup>15</sup>N-separated [<sup>1</sup>H,<sup>1</sup>H]NOESY (33), four-dimensional (4D) <sup>13</sup>C/<sup>15</sup>N-separated [<sup>1</sup>H,<sup>1</sup>H]NOESY (34), and 4D <sup>13</sup>C/<sup>13</sup>C-separated [<sup>1</sup>H,<sup>1</sup>H]NOESY (35) experiments, the latter in D<sub>2</sub>O. The mixing time for the 3D <sup>15</sup>N-separated [<sup>1</sup>H,<sup>1</sup>H]NOESY experiment was 100 ms, and for 4D spectra, the mixing time was 65–70 ms. In all experiments, an acquisition time of 15–20 ms and 30–40 complex points (7.2 ms and 14 complex points for the 4D experiment) were used in the <sup>15</sup>N dimension and an acquisition time of 22.9 ms and 256 complex points were used in the observed dimension. The acquisition time and number of complex points in the remaining dimension(s) as well as the number of scans per hypercomplex increment were as follows: 23.2 ms and 42 complex points on the 600 MHz spectrometer (24 scans) for HNCO, 9.2 ms and 48 complex points (32 scans) for HNCA, 6.3 ms and 48 complex points (24 scans) for CBCA(CO)-NH, 5.3 ms and 56 complex points (32 scans) for HNCACB, 4.2 ms and 40 complex points (32 scans) for (H)-C-(CCO)-NH, 10.2 ms and 46 complex points (32 scans) for HBHA-(CBCACO)NH, 8.75 ms and 70 complex points (16 scans)

for 3D <sup>15</sup>N-separated [<sup>1</sup>H,<sup>1</sup>H]NOESY, and 7.5 ms and 60 complex points for the <sup>1</sup>H dimension and 2.9 ms and 14 complex points for the <sup>13</sup>C dimension (four scans) for 4D <sup>13</sup>C/<sup>15</sup>N-separated [<sup>1</sup>H,<sup>1</sup>H]NOESY. For the 4D <sup>13</sup>C/<sup>13</sup>C-separated [<sup>1</sup>H,<sup>1</sup>H]NOESY experiment, the acquisition time and the number of complex points were 10.8 ms and 54 for the <sup>1</sup>H dimension and 2.5 ms and 10 for each <sup>13</sup>C dimension (12 scans). <sup>3</sup> $J_{\alpha N}$  coupling constants were estimated using the 3D HNHA experiment (36) with an acquisition time of 9.3 ms and 52 complex points (16 scans). This experiment used a dephasing period of 19 ms, and  $J$  values were scaled by a factor of 1.2 to account for <sup>1</sup>H spin flips during the dephasing and rephasing periods (36). 2D [<sup>1</sup>H,<sup>15</sup>N]TROSY-HSQC (37) spectra were recorded in a manner similar to that of the non-TROSY experiment. Triple-resonance NMR experiments involving detection of amide protons used the enhanced sensitivity approach, achieving coherence pathway transfer selection with pulsed field gradients. The acute effects of solvent exchange at pH 8 were mitigated by employing a series of selective flipback pulses on the water resonance, thereby keeping water magnetization aligned along the  $z$ -axis throughout the experiment and minimizing the effects of solvent exchange on amide protons as described previously (38, 39). Alternatively, the WATERGATE (WATER suppression by gradient-tailored excitation) or 3-9-19 sequences (40, 41) were applied. For D<sub>2</sub>O-exchange experiments, 0.35 mM unlabeled IFNAR2-EC was diluted 3-fold with D<sub>2</sub>O-based 25 mM Tris (pH 8) containing 0.02% NaN<sub>3</sub>, and then concentrated back to its initial volume in a Fugisep concentration tube. This process was repeated four times and was completed in less than 90 min. The sample was immediately transferred to the previously tuned and shimmed 800 MHz spectrometer. Short 2D NOESY experiments with an acquisition time of 10 ms, 200 complex points, 16 scans per hypercomplex points, and a mixing time of 80 ms (total experiment time of 3.5 h) were then carried out successively. Amide proton cross-peaks detected 10 h later were considered to be slowly exchanging, and assigned using the characteristic NOE interactions between the amide proton and its two neighboring H $\alpha$  protons.

Typical carrier positions for all experiments were 118 ppm for <sup>15</sup>N, 176 ppm for <sup>13</sup>CO, 55 ppm for <sup>13</sup>C $_{\alpha}$ , 45 ppm for <sup>13</sup>C $_{\alpha}$ /<sup>13</sup>C $_{\beta}$ , and 4.67 ppm for <sup>1</sup>H. For TROSY experiments, the <sup>15</sup>N carrier was shifted to 118.5 ppm to facilitate later comparison with non-TROSY experiments. A DIPSI-2 train pulse (42) was used for the <sup>13</sup>C TOCSY experiment. A WALTZ-16 (43) train pulse was used for proton and deuterium decoupling, and a GARP (44) train pulse was used for heteronuclear decoupling. Selective <sup>13</sup>C pulses were applied as soft G4- and G3-shaped pulses or rectangular pulses at 6.5 and 13.9 kHz for 90° and 180° pulses, respectively. Data were acquired in the States–TPPI mode for the <sup>13</sup>C dimension in triple-resonance experiments or the indirect <sup>1</sup>H dimension in NOESY-type experiments (45) or Echo-Antiecho (for the <sup>15</sup>N dimension of sensitivity-enhanced or TROSY experiments) (46) as required for quadrature detection. Chemical shifts were referenced as described previously (47).

**NMR Measurements for the IFNAR2-EC–IFN- $\alpha$ 2 Complex.** NMR data for IFNAR2-EC in complex with unlabeled IFN- $\alpha$ 2 were measured at 40 °C. The 2D [<sup>1</sup>H,<sup>15</sup>N]TROSY-HSQC (37) and 3D HNCA-TROSY experiments were



carried out using a  $^{13}\text{C}$ - and  $^{15}\text{N}$ -labeled IFNAR2-EC–U-IFN- $\alpha 2$  complex, and the 3D HNCACB-TROSY experiment (48) was carried out using a 50%- $^2\text{H}$ ,  $^{13}\text{C}$ ,  $^{15}\text{N}$ -IFNAR2-EC–U-IFN- $\alpha 2$  complex. Data for the  $^{15}\text{N}$  and observed dimensions were acquired as described for free IFNAR2-EC. Acquisition times and the number of complex points as well as the number of scans per hypercomplex point for the  $^{13}\text{C}$  dimension of these experiments were as follows: 6.1 ms and 32 complex points (40 scans) for HNCA-TROSY and 1.8 ms and 20 complex points (176 scans) for HNCACB-TROSY. For  $\text{D}_2\text{O}$ -exchange experiments, 0.25 mM  $^{15}\text{N}$ -labeled IFNAR2-EC complexed with unlabeled IFN- $\alpha 2$  was transferred to  $\text{D}_2\text{O}$ -based buffer as described for free IFNAR2-EC. 2D  $[^1\text{H}, ^{15}\text{N}]$ TROSY-HSQC experiments with 60 scans per hypercomplex point (total experiment time of 4.5 h) were then carried out successively as described earlier. Amide proton cross-peaks detected 10 h later were considered to be slowly exchanging.

**Modeling IFNAR2-EC.** The sequences of of hCRII extracellular domains with available three-dimensional structures were aligned against the IFNAR2-EC sequence using the CLUSTALW program. The models for the N-terminal and C-terminal FN-III domains of IFNAR2-EC were based on the three-dimensional structures of the homologous TFR N-terminal domain (22% sequence identity, PDB entry 1FAK at 2.10 Å resolution) and IFN $\gamma$ R C-terminal domain (17% sequence identity, PDB entry 1FYH at 2.04 Å resolution), respectively. Alignment of IFNAR2-EC and superposition of the two template structures, as well as all steps toward refinement of the final model, were performed using the InsightII software package (Accelrys). Random loop generation was performed using the Homology module, and refinement of the model using iterative energy minimization and dynamics steps employed the Discover3 and Biopolymer modules.

## RESULTS

**Backbone Assignments for Free and Complexed IFNAR2-EC.** Standard multidimensional NMR spectra were applied to assign backbone resonance frequencies of free and complexed IFNAR2-EC. Figure 1 exemplifies the “sequential walk” in the HNCACB spectrum along the polypeptide chain for free IFNAR2-EC, demonstrating the methodology used to link adjacent residues and assign backbone chemical shifts using triple-resonance experiments. More than 90% of the amide protons of free IFNAR2-EC (183 of 201 non-proline residues) could be assigned using these data. In assigning backbone nuclei of the IFNAR2-EC–IFN- $\alpha 2$  complex, we made use of the high level of similarity between 2D  $[^1\text{H}, ^{15}\text{N}]$ TROSY-HSQC spectra of free and IFN- $\alpha 2$ -bound IFNAR2-EC as described below. The TROSY-HNCA experiment (48), normally insufficient for backbone assignment of a 43 kDa protein because of the low dispersion of  $^{13}\text{C}_\alpha$  chemical shifts and their weak correlation to residue type, was used to verify the identity of residues whose  $^1\text{H}$  and  $^{15}\text{N}$  chemical shifts remained unchanged upon formation of the complex. Together with the TROSY-HNCACB experiment, more than 85% of the amide protons of the IFNAR2-EC–IFN- $\alpha 2$  complex (172 of 201 non-proline residues) could be assigned using these data. In both cases, unassigned residues were invariably located in  $\beta$ -turns or unstructured loops as postulated by NMR data, mobile regions subject to

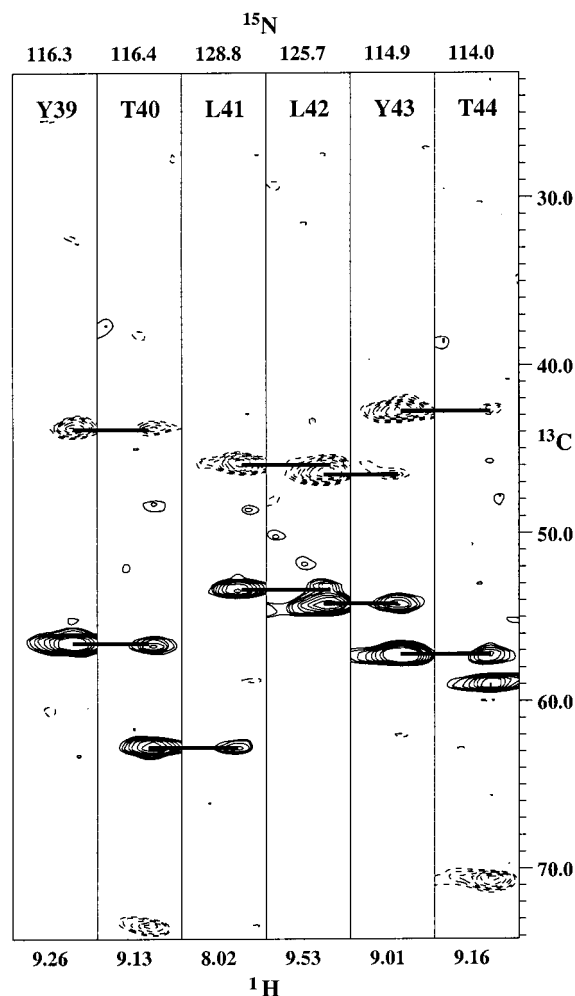


FIGURE 1: Sequential walk along the HNCACB spectrum for IFNAR2-EC. Strips taken from the HNCACB spectrum acquired for 0.35 mM uniformly  $^{13}\text{C}$ - and  $^{15}\text{N}$ -labeled IFNAR2-EC in 25 mM Tris (pH 8) and 0.02%  $\text{NaN}_3$  at 35 °C. Each strip represents the correlations of a backbone amide  $^1\text{H}$ – $^{15}\text{N}$  pair with two  $^{13}\text{C}_\alpha$  nuclei and two  $^{13}\text{C}_\beta$  nuclei. Alignment of intra- and interresidue correlations arranges the strips sequentially and allows assignment. This is demonstrated for residues Y39–T44, with horizontal bars connecting peaks with identical  $^{13}\text{C}$  shifts establishing the sequential connectivities. The  $^{13}\text{C}_{\beta^1-1}$  peak of L41 is below the plotted contour level.

rapid solvent exchange and consequent line broadening. Significantly, all amide protons forming hydrogen bonds in the postulated  $\beta$ -sheets were detectable. Despite these difficulties, levels of backbone assignment are satisfactory when considering the high pH of the sample, and comparable to those previously reported under similar measurement conditions (39).

**Secondary Structure and Global Fold of IFNAR2-EC.** Several NMR-derived parameters are closely correlated to protein secondary structure, and are therefore reliable predictors of such motifs in polypeptides. Most prominent are the deviation of chemical shifts from random coil values (49),  $^3J_{\text{N}\alpha}$  coupling constants and characteristic sequential and medium-range NOE connectivities, as well as  $\text{D}_2\text{O}$ -exchange data (50). Figure 2 summarizes these NMR parameters and suggested structural motifs for IFNAR2-EC. These data suggest the existence of 14  $\beta$ -strands (seven in each immunoglobulin domain) as expected for receptors of this family. N-Terminal subdomain  $\beta$ -strands were formed by

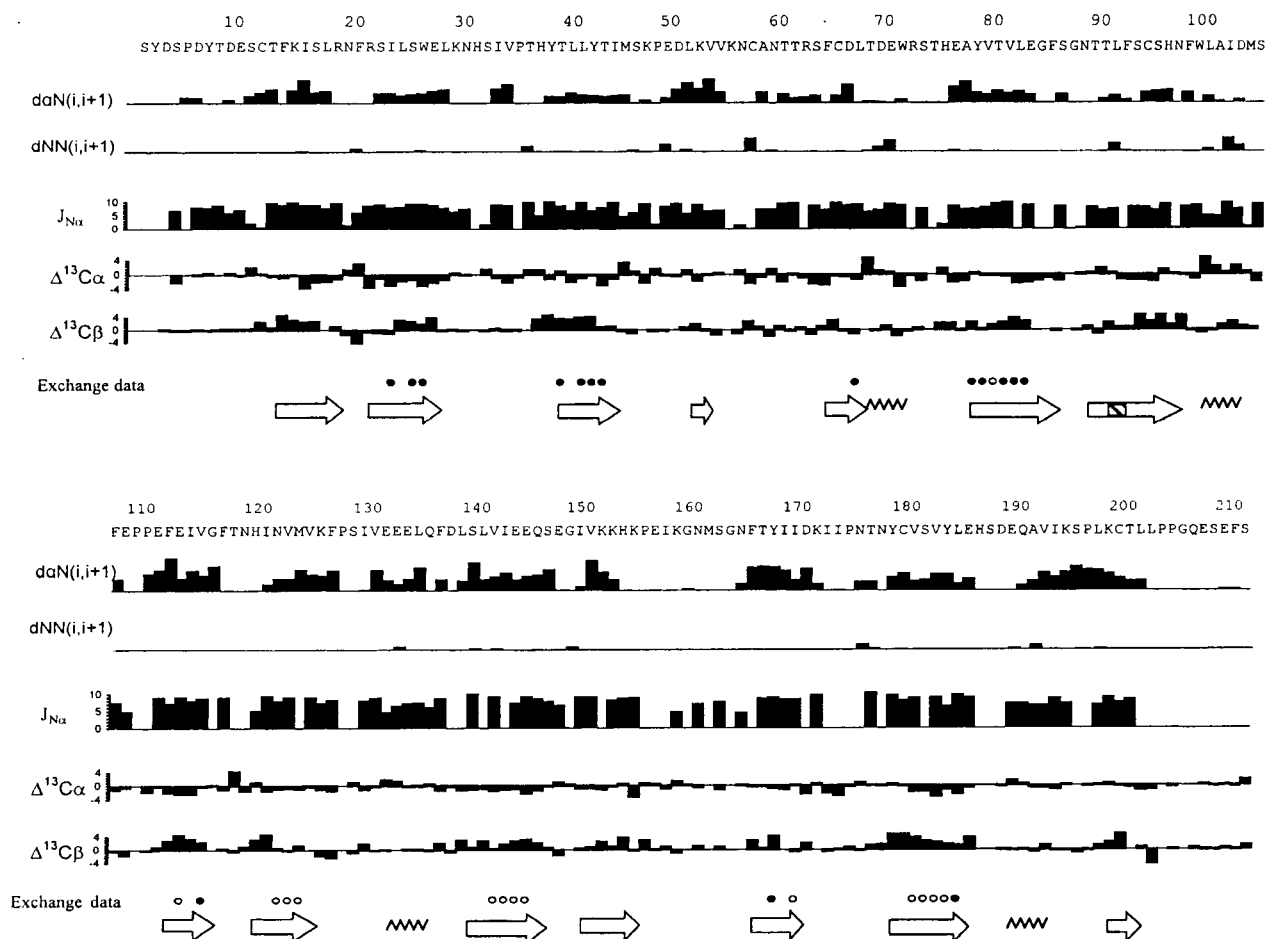


FIGURE 2: Secondary structure data for IFNAR2-EC. Summary of all data for sequential NOEs involving the  $H^N$  and  $H^\alpha$  protons,  $^3J_{N\alpha}$  couplings,  $^{13}C_\alpha$  and  $^{13}C_\beta$  secondary shifts, and  $D_2O$ -exchange rates observed for residues of IFNAR2-EC.  $J$  couplings were estimated where possible using the 3D HNHA experiment. NOE interactions were extracted from the 3D  $^{15}N$ -separated and 4D  $^{13}C/^{15}N$ -separated NOESY spectra. Empty circles denote amide protons detectable 10 h after exposure of free IFNAR2-EC to  $D_2O$ . Filled circles denote amide protons unobserved in free IFNAR2-EC but detected in the IFNAR2-EC-IFN- $\alpha 2$  complex (all slowly exchanging protons in free IFNAR2-EC were observed in the complex as well). The suggested secondary structure appears below the data, with  $\beta$ -strands and helices represented by arrows and sawtooth patterns, respectively. The  $\beta$ -bulge in strand S7 is represented by a hatched box.

segments of residues 13–19, 22–28, 39–45, 53–55, 65–68, 79–87, and 90–99, the latter including a  $\beta$ -bulge at residues 91–93. C-Terminal subdomain  $\beta$ -strands were formed by segments of residues 112–117, 120–125, 140–147, 150–155, 166–170, 179–186, and 199–202. Location of  $\beta$ -sheets is consistent with the fact that all slowly exchanging amide protons of free IFNAR2-EC and the IFNAR2-EC-IFN- $\alpha 2$  complex (observable after exposure to  $D_2O$  for 8–12 h) are included in these segments. The spatial arrangement of the 14 established  $\beta$ -strands was determined using multidimensional heteronuclear-separated NOESY experiments. Connectivities obtained from these experiments (50–60 in each subdomain) established the global fold for both subdomains, and assisted in determining the borders of  $\beta$ -strands in cases of ambiguity. Figure 3 demonstrates the fold established for IFNAR2-EC. Both subdomains possess very similar topological features, and can be classified as type s immunoglobulin folds (51), each containing seven  $\beta$ -strands arranged in two sheets with an all-antiparallel configuration. Tight turns were identified by their characteristic NOE fingerprint and seen for segments of residues 19–22, 87–90, 117–120, and 147–150. Residues in the second and third positions of such turns are typically exposed to solvent exchange, accounting for the

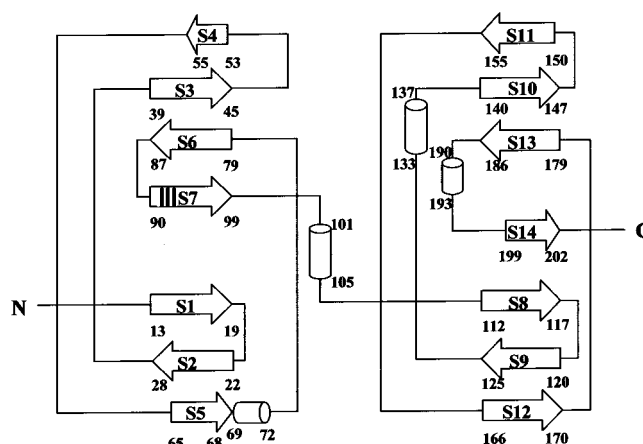


FIGURE 3: Secondary structure and global fold of IFNAR2-EC. A schematic representation of the topology of IFNAR2-EC shows its double immunoglobulin fold. Sequentially numbered  $\beta$ -sheets appear as arrows, and helices are depicted as cylinders. Disulfide bonds are not shown, and selected residues are numbered for clarity.

absence of amide protons of residues N20, G88, N89, and N119 from the HSQC spectrum. The presence of Gly or Asn residues at the apex of such turns is highly characteristic (52). NOE data indicate that the S7  $\beta$ -strand is interrupted

|               |   |     |
|---------------|---|-----|
| <b>IFNAR2</b> | SYDSPDYTDESC <b>TFKISLRNFRSILSWE</b> LKN--HSIVPTHY <b>TLTYTIMSKPEDLKVV</b> KNCANT                                     | 61  |
| <b>TFR</b>    | -----NTVAAYNL <b>TKSTNFKTILEWE</b> -----PKPVNQ <b>VYTVQIST</b> -----KSGDW <b>KSK</b> CFYT                             | 52  |
| <b>IFNγR</b>  | ADLGPSVPTPT <b>NTVTIESYNMNP</b> <b>IVYWE</b> YQ---IMPQVP <b>VFTVEVK</b> NYGV-KNSEWID <b>ACINI</b>                     | 66  |
|               | S1 S2 S3 S4   |     |
| <b>IFNAR2</b> | TRSF <b>CDL</b> <b>TDE</b> NRST-HEAY <b>YTV</b> LE <b>GFS</b> -GN----- <b>TTLFSCSHNFW</b> L <b>AIDMS</b> FEEPP        | 110 |
| <b>TFR</b>    | TDTE <b>CDL</b> <b>TDE</b> IVKDV <b>KQTYLARVFSYP</b> AGNVESTGSAGEPL <b>YENS</b> PEFT <b>PYLE</b> TNLGQP               | 111 |
| <b>IFNγR</b>  | SHH <b>YCN</b> <b>SDHV</b> GDP-SNS <b>LWVRVK</b> ARV-GQ----- <b>KE</b> SAY <b>AK</b> SEEF <b>AVCR</b> DGKIGPP         | 116 |
|               | S5 H1 S6 S7 H2  |     |
| <b>IFNAR2</b> | <b>EFE</b> IV <b>GFT</b> - <b>NHINVM</b> KFPSIV----- <b>EELQF</b> ----- <b>DLSLV</b> IE <b>EQSE</b> -                 | 148 |
| <b>TFR</b>    | <b>TIQSFE</b> QVG <b>TKVNV</b> TVEDERTLVRNNT <b>FLSL</b> <b>RDVF</b> ----- <b>GKDL</b> I <b>YTL</b> Y <b>Y</b> WKS    | 160 |
| <b>IFNγR</b>  | <b>KLD</b> IRKEE- <b>KQIM</b> ID <b>IFHP</b> ----- <b>SVF</b> VNGDEQ <b>EV</b> DYDPETTCY <b>IRV</b> NY <b>VVRM</b>    | 164 |
|               | S8 S9 H3 S10  |     |
| <b>IFNAR2</b> | ---GIV <b>KKH</b> KPEIKGNM--SGN <b>FTY</b> IIDKLIPN-TNY <b>CVSV</b> YLEHS <b>DEQA</b> VIKSPL--- <b>KCTL</b>           | 202 |
| <b>TFR</b>    | SSSG <b>KKTAK</b> TN-----TNE <b>FL</b> IDVDKG---ENY <b>CF</b> SV <b>QAV</b> IPSR <b>TVNR</b> KSTDS <b>PVE</b> CM-     | 211 |
| <b>IFNγR</b>  | N--G <b>SEI</b> Q <b>YKIL</b> TQKEDDCDEI <b>QCQLA</b> IPVSS <b>LNSQYCV</b> SA <b>EGVL</b> HVWGVTTEKSK-- <b>EV</b> CIT | 220 |
|               | S11 S12 S13 H4 S14  |     |
| <b>IFNAR2</b> | LPPGQESEFS  | 212 |
| <b>TFR</b>    | -----   | 211 |
| <b>IFNγR</b>  | IFNSSIKGS-  | 229 |

FIGURE 4: Sequence alignment of IFNAR2-EC. The sequences of IFNAR2-EC and related receptor extracellular domains were aligned using the  $\beta$ -strands predicted by NMR data and additional structural data (details in the text). Residues in  $\beta$ -strands appear in boldface and are based on PDB entries 1FAK from ref 20 and 1FYH from ref 19 for TFR and IFN $\gamma$ R, respectively. Helical segments are italicized and underlined. The double-proline motif of the interdomain hinge and the conserved cysteines are boxed. Secondary structure motifs of IFNAR2-EC are sequentially numbered S1–S14 and H1–H4. Amino acids are numbered 1–212 for IFNAR2-EC, 1–211 for TFR, and 9–229 for IFN $\gamma$ R. Residues prior to the IFNAR2-EC N-terminus are omitted for clarity.

by a  $\beta$ -bulge at residues 91–93. This is supported by the sequential  $H_N$ – $H_N$  interaction observed for residues 92 and 93 and the strong interaction between F93  $H_N$  and T91  $H_\alpha$ . In addition, the  $^{13}C_\alpha$  and  $^{13}C_\beta$  chemical shifts of T91 and L92 are inconsistent with a  $\beta$ -conformation. The appearance of inter- $\beta$ -strand NOEs between residues E84 and S94 ( $H_\alpha$ – $H_\alpha$ ) indicates they return to form a  $\beta$ -sheet. Sequential  $H_N$ – $H_N$  and typical  $H_\alpha^i$ – $H_N^{i+2}$  or  $H_\alpha^i$ – $H_N^{i+3}$  NOE interactions are observed for the short segments including residues 69–72, 101–105 (the interdomain hinge region), 133–137, and 190–193, suggesting they adopt helical conformations (50).

**Modeling the Structure of IFNAR2-EC.** Homology modeling of IFNAR2-EC suffers from the low levels of identity IFNAR2-EC exhibits with related receptors and other FN-III domains. We therefore utilized the NMR-derived secondary structure information to improve the alignment of IFNAR2-EC and template structures. In this structural alignment, secondary structure motifs obtained from our NMR study were aligned with known structural elements in the templates, and structural similarity was generally preferred over sequence homology in segments with contradictory alignments. The resulting alignment used for modeling IFNAR2-EC is shown in Figure 4. The two template structures that are most similar to IFNAR2-EC, TFR and

IFN $\gamma$ R, were chosen for purposes of coordinate assignment and modeling. On the basis of the structural similarity and location of  $\beta$ -strands and loops throughout the domains, the N-terminal (residues 1–106) and C-terminal (residues 107–212) domains of IFNAR2-EC were assigned the coordinates of the N-terminal domain of TFR and the C-terminal domain of IFN $\gamma$ R, respectively. The two domains were then linked, maintaining the interdomain angle characteristic of the hCR2 family, and all refinement steps were applied to modeled IFNAR2-EC as a whole. NMR-derived constraints, including interproton distances, established hydrogen bonds, and dihedral constraints, were applied during the refinement process, ensuring the consistency of the calculated model with experimental NMR data. This modeled structure of IFNAR2-EC is shown in Figure 5. The proposed model features the double-FN-III domain fold with a characteristic arrangement of  $\beta$ -sheets and helical segments commonly observed in the hCR2 family. The C12–C95 disulfide bond, unique to IFNAR2-EC among hCR2 extracellular domains, bridges the  $\beta$ -sheets in the N-terminal domain correctly and maintains the proper orientation of hydrophilic and hydrophobic side chains in the S1  $\beta$ -strand on the edge of the  $\beta$ -sheet. In addition, 95% of the backbone angles of the IFNAR2-EC model are within the allowed regions of the

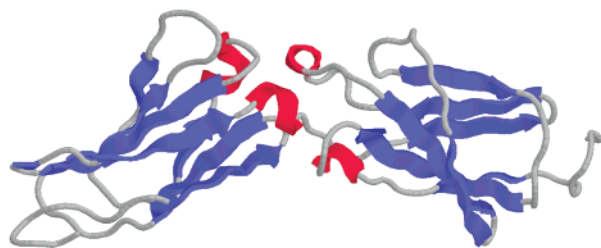


FIGURE 5: Modeled structure of IFNAR2-EC. The NMR-derived homology model of IFNAR2-EC is presented.  $\beta$ -Strands are depicted as blue arrows and helices as red coils. This figure was generated using Rasmol.

Ramachandran plot. This model has pairwise rmsd values of 3.7 and 6.3 Å for the N- and C-terminal domains, respectively, when compared to a previously suggested model (11). The C-terminal domain exhibits a lower sequence identity level, resulting in a larger contribution of the structural alignment and accounting for its higher rmsd value. Overall, the introduction of NMR-derived data and constraints into the modeling process has alleviated the difficulties presented by low homology levels and resulted in an improved modeled structure for IFNAR2-EC.

**Mapping of the IFN- $\alpha$ 2 Binding Site on IFNAR2.** Differences in chemical shift are indicative of a changing chemical environment, and are therefore useful in following the formation of complexes. Once the assignment of backbone nuclei is completed, such changes accompanying complex formation can be traced to specific residues and related to structural elements. Analysis of these changes enables us to map the binding site in such a complex (53). We applied the 2D [ $^1\text{H}$ , $^{15}\text{N}$ ]TROSY-HSQC (37) experiment to the IFNAR2-EC–IFN- $\alpha$ 2 complex, in which only IFNAR2-EC was labeled with  $^{15}\text{N}$ . Strikingly, 85% of the  $^1\text{H}$ – $^{15}\text{N}$  cross-peaks exhibited little or no change in chemical shifts when compared to free IFNAR2-EC, making this method an excellent tool for probing structural aspects of the binding site of IFNs. Figure 6 compares the TROSY-HSQC spectra for free and complexed IFNAR2-EC. When plotted against their position along the polypeptide chain, these changes in chemical shift upon IFN- $\alpha$ 2 binding localize to three well-defined regions as shown in Figure 7, allowing several structural conclusions to be drawn. Residues unaffected by IFN- $\alpha$ 2 binding encompassed the S1–S2–S5  $\beta$ -sheet in the N-terminal subdomain, and essentially the entire C-terminal subdomain. Binding of IFN- $\alpha$ 2 resulted in large changes in chemical shift (defined as a weighted change exceeding 0.2 ppm; see Figure 7) or unassignable triple-resonance cross-peaks for 29 residues. The three main regions of change in chemical shift are residues T44–K53 (the S3–S4 loop), S74–V82 (the S5–S6 loop and adjacent S6  $\beta$ -strand), and C95–M105 (the S7 strand and interdomain hinge region helix), all corresponding to binding hot spots reported in cellular and biophysical studies. Residues giving rise to weak cross-peaks in free IFNAR2-EC were often undetectable in the spectra of the complex, and their absence in the spectra of the complex must be attributed to low signal to noise rather than to the effects of ligand binding. Other residues implicated in IFN- $\alpha$ 2 binding such as K48 and I103 could not be assigned for reasons stated above, and the amide proton of H76 was undetectable even for free IFNAR2-EC. Another finding is the minute contribution of the C-terminal

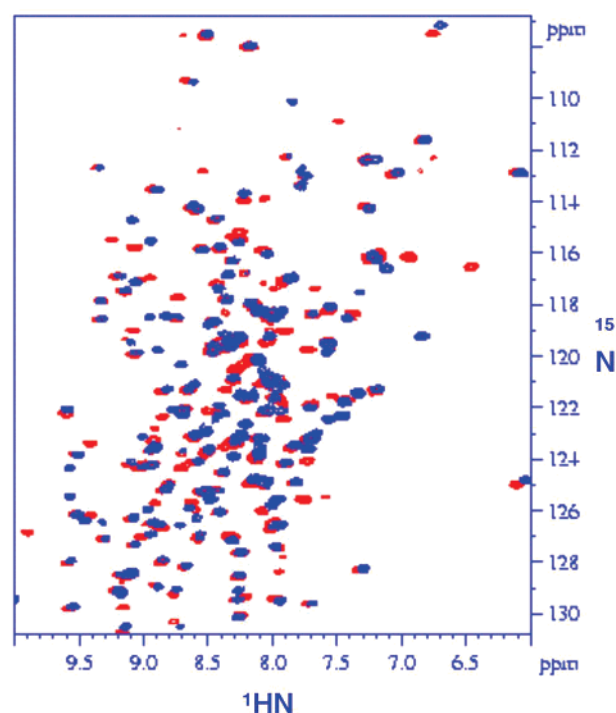


FIGURE 6: Effects of IFN- $\alpha$ 2 binding on the chemical shifts of IFNAR2-EC. Shown is an overlay of the 2D [ $^1\text{H}$ , $^{15}\text{N}$ ]TROSY-HSQC spectra for free IFNAR2-EC (blue) and its complex with IFN- $\alpha$ 2 (red). Spectra were acquired on a DRX 800 MHz spectrometer (Bruker) for 0.35 mM uniformly  $^{13}\text{C}$ - and  $^{15}\text{N}$ -labeled IFNAR2-EC and 0.25 mM  $^{15}\text{N}$ -IFNAR2-EC–U-IFN- $\alpha$ 2 complex, both in 25 mM Tris (pH 8) and 0.02%  $\text{NaN}_3$  at 35 °C.

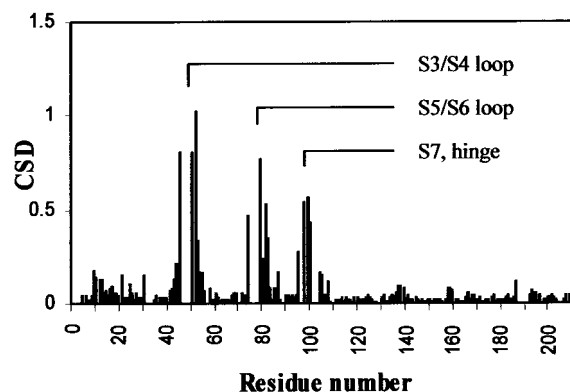


FIGURE 7: Position of chemical shift deviations induced by IFN- $\alpha$ 2 binding along IFNAR2-EC. Comparison of chemical shifts in the 2D [ $^1\text{H}$ , $^{15}\text{N}$ ]TROSY-HSQC spectra for free IFNAR2-EC and its complex with IFN- $\alpha$ 2. Shown are the chemical shift deviations (CSD) as a function of residue number. CSD values were calculated using the formula  $\sqrt{[\Delta(\delta\text{H})]^2 + \Delta(\delta\text{N}/5)^2}$ , where  $\Delta(\delta\text{H})$  and  $\Delta(\delta\text{N})$  are the changes in  $^1\text{H}$  and  $^{15}\text{N}$  chemical shifts, respectively. Missing values indicate cross-peaks that cannot be assigned for free or complexed IFNAR2-EC or Pro residues. Three major regions of change, corresponding to three segments forming the IFN- $\alpha$ 2 binding site, are appropriately labeled.

subdomain to the interaction with IFN- $\alpha$ 2. The only region affected by IFN- $\alpha$ 2 binding is the helical segment of residues 190–194. While a significant change in chemical shifts is not exhibited, a noticeable attenuation in signal occurs for amide protons of these residues. Cross-peaks of residues 192–194 are weak in the TROSY-HSQC spectra, and those of residues 190 and 191 are absent. The binding site mapped





FIGURE 8: Mapping of the IFN- $\alpha$ 2 binding site upon IFNAR2-EC. Results of the mapping analysis are juxtaposed on the modeled structure of IFNAR2-EC and compared to mutagenesis studies. At the left are labeled and shown in green residues implicated by mutagenesis in binding of IFN- $\alpha$ 2. At the right are highlighted residues exhibiting significant change in chemical shifts upon complex formation. The three segments forming the contiguous binding surface are shown in different shades of green. Unassigned residues within the affected regions are highlighted as well.

by this analysis of chemical shift deviations is consistent with the results of mutagenesis studies, as shown in Figure 8.

**IFN- $\alpha$ 2-Induced Structural Change in IFNAR2-EC.** D<sub>2</sub>O-exchange measurements performed on the <sup>15</sup>N-IFNAR2-EC-IFN- $\alpha$ 2 complex were instrumental in further characterizing the complex and the structural implications of ligand binding. IFN- $\alpha$ 2 binding was shown by these experiments to have a strong effect on the kinetics of solvent exchange of IFNAR2-EC amide protons. In free IFNAR2-EC, a total of 14 slowly exchanging amide protons are detected, only one of which is located on the N-terminal subdomain. In contrast, in the IFNAR2-EC-IFN- $\alpha$ 2 complex, 32 such protons are detected, and the N-terminal domain contains 15 of these, as indicated by the exchange data depicted in Figure 2. Therefore, the vast majority of amide protons protected from exchange by IFN- $\alpha$ 2 binding (14 of 17) are concentrated in the N-terminal subdomain. All of the slowly exchanging protons in both subdomains are located within  $\beta$ -sheets determined by NMR data for free IFNAR2-EC, and more than 80% are located in inner  $\beta$ -strands of the  $\beta$ -sheets, e.g., in the S2, S3, S6, S9, S10, or S13 strands.

## DISCUSSION

**Structural Comparison of IFNAR2-EC and Related Cytokine Receptors.** In this study, we determine the global fold of IFNAR2-EC for the first time using state-of-the-art multidimensional NMR techniques. The global fold and additional structural considerations were used to align the sequence of IFNAR2-EC with those of the related receptors TFR and IFN $\gamma$ R, enabling us to calculate an improved model for the structure of IFNAR2-EC. The NMR-determined topology of IFNAR2-EC is generally similar to the folds exhibited by these polypeptides. The short helical segments of IFNAR2-EC can all be compared to homologous motifs in other members of the hCR2 family. The helices at residues 69–72 and 101–105 are common to all receptors of this class, and the helix at residues 133–137 has homologues in both TFR and IFN $\gamma$ R. While absent in many members of the hCR2 family, the helix at residues 190–193 has been observed in the interleukin-4 receptor (IL-4R). The  $\beta$ -sheet topology of IFNAR2-EC is also highly characteristic of the hCR2 family, particularly in the conserved  $\beta$ -sheets comprised of strands S1, S2, and S5 in the N-terminal FN-III domain and strands S8, S9, and S12 in the C-terminal

domain. Certain differences, however, should be mentioned. The short S4  $\beta$ -strand of IFNAR2-EC (residues 53–55) is similar to the homologous strand in GHR and the TFR sequence used for modeling, but other TFR sequences and IFN $\gamma$ R have a longer strand, encompassing the conserved Cys residue. Therefore, the conserved disulfide bond (C49–C57 and C63–C71 for TFR and IFN $\gamma$ R, respectively) tightly constrains the two  $\beta$ -sheets of this domain. In contrast, the S4–S5 loop of IFNAR2-EC is longer and the C58–C66 disulfide bond less constraining. The amide protons of K56 and N57 of IFNAR2-EC were unobservable in triple-resonance spectra, supporting the proposition that they are solvent-exposed and part of the flexible loop that traverses the gap between the two  $\beta$ -sheets. This difference between IFNAR2-EC and its hCR2 counterparts is expected to affect the relative positioning of the  $\beta$ -sheets in the N-terminal domain, and therefore also the structure of the ligand binding sites. Another important contribution of the NMR data is at the S9–S10 loop, which has posed difficulties in previous homology modeling studies (10, 11), since it contains the largest deletion in IFNAR2-EC sequence when aligned against TFR and IFN $\gamma$ R. NMR-derived parameters precisely locate this loop at residues 126–139, including the helical segment at residues 133–137. One interesting feature of the proposed model for IFNAR2-EC is the  $\beta$ -bulge in the S7 strand, including residues 91–93. The backbone of this segment adopts a polyproline helix conformation exhibited by the well-known WSXWS box characteristic of the last  $\beta$ -strand of the C-terminal FN-III domain of the hCR1 family. A similar motif is homologously located in the N-terminal domain of IFN $\gamma$ R. Significantly, this segment in both receptors shares some degree of sequence homology with the WSXWS motif (TTLFS and ESAYA in IFNAR2-EC and IFN $\gamma$ R, respectively). These findings clearly demonstrate the capabilities of NMR in complementing, extending, and refining currently available structural information regarding the IFNAR-IFN system.

**Identification of the IFN- $\alpha$ 2 Binding Site on IFNAR2-EC.** Deviations in backbone NH chemical shifts between free and complexed IFNAR2-EC were used in this study to identify the binding site of IFN- $\alpha$ 2 on its receptor. This mapping method is very informative in cases where the changes in chemical shift are localized in the binding site, and the majority of residues remain unaffected by binding. The



IFNAR2-EC-IFN- $\alpha$ 2 system is therefore perfectly suited for application of this method, since the chemical shifts of 85% of its residues are unaffected by IFN- $\alpha$ 2 binding. Our results establish three domains that form the IFN- $\alpha$ 2 binding surface on IFNAR2-EC: the S3-S4 loop, including the TIMSK motif (residues 43-53); the S5-S6 loop and the S6  $\beta$ -strand, including the HEAY motif (residues 74-82); and the interdomain hinge and adjacent residues in the S7  $\beta$ -strand (residues 95-105). The three protruding loops along with the helical interdomain hinge are shown by the IFNAR2-EC model to form a contiguous surface upon the N-terminal immunoglobulin domain accessible to IFN- $\alpha$ 2. The contribution of  $\beta$ -strands to ligand binding differentiates this family of receptors from antibodies, where the antigen-binding site is formed by loops alone. The binding site also handsomely overlaps regions previously implicated in IFN- $\alpha$ 2 binding. Site-directed mutagenesis and immunoblocking studies of cellular IFNAR2 established significant contributions to IFN- $\alpha$ 2 binding for residues T44, M46, and K48 of the S3-S4 loop, H76, E77, and Y79 of the S5-S6 loop and S6  $\beta$ -strand, and W100, I103, and D104 of the interdomain hinge region (10-12). Mutational studies of the kinetics and thermodynamics of IFNAR2-EC-IFN- $\alpha$ 2 complex formation found additional contributions for residues I45 and S47 as well (11). Deviations in chemical shift for residues on the periphery of the binding site are expected due to the long-range character of factors influencing chemical shift, but an indirect contribution to binding by these residues cannot be ruled out. Although chemical shift deviations should generally be interpreted only qualitatively, most deviations may be explained in structural terms based upon the proximity of specific residues to the binding site and the topology established by NMR. Thus, residue Y79 is part of the HEAY motif strongly implicated in IFN- $\alpha$ 2 binding, and it exhibits one of the largest deviations in chemical shift. The NH moiety of T81 is co-oriented by the  $\beta$ -structure with that of Y79, accounting for its larger deviation, as opposed to residues V80 and V82 which face the opposite direction and experience more moderate changes. W100 is another residue contributing significantly to IFN- $\alpha$ 2 binding, and together with the adjacent F99 exhibits large chemical shift changes, while those of C95, D104, or M105 are less pronounced. Similar profiles of change in chemical shift upon IFN- $\alpha$ 2 binding were observed for the  $^{13}\text{C}_\alpha$  and  $^{13}\text{CO}$  nuclei (data not shown).

NMR data also exhibit an attenuation of signals originating from residues in the helical segment of residues 190-194, beyond that expected for the increase in the molecular mass upon complex formation. Since the intensities of other cross-peaks do not exhibit this effect to such an extent, the observed attenuation should be attributed to local binding-induced causes. This region has been previously shown to participate in GHR binding of its ligand (23), and is proximal to the interdomain hinge in the IFNAR2-EC model. Site-directed mutagenesis has suggested only minor involvement of E190 in ligand binding (10, 11). A possible explanation for the NMR findings is that IFN- $\alpha$ 2 binding affects the helical character of this segment and exposes it to solvent exchange.

Comprehensive mapping of the IFN- $\alpha$ 2 binding site upon IFNAR2-EC suffers from the relative insensitivity of triple-resonance experiments required for backbone assignment

when applied to the 50% deuterated 43 kDa IFNAR2-EC-IFN- $\alpha$ 2 complex. However, all unassigned correlations were analyzed and compared to those of missing residues, establishing a lower limit for their deviation in chemical shift. All unassigned residues located in regions exhibiting large chemical shift deviations were thus shown to participate in the IFN- $\alpha$ 2 binding site. The binding site of IFN- $\alpha$ 2 upon its receptor suggested by NMR is in excellent agreement with results of previous studies, forming a binding surface on the N-terminal FN-III domain and including the S13-S14 loop which exhibits a minor contribution to binding. This correlation between the NMR data and previously reported biological findings emphasizes the utility of this approach in the study of structural aspects of the IFNAR2-EC-IFN- $\alpha$ 2 complex and other IFN complexes.

*Tightening of the IFNAR2-EC Structure upon IFN- $\alpha$ 2 Binding.* The binding site mapping of IFNAR2-EC clearly determines that IFNAR2-EC does not experience a global conformational change upon IFN- $\alpha$ 2 binding. IFNAR2-EC exhibits large localized changes in chemical shifts, as opposed to smaller changes throughout the sequence that have been observed in other complexes (54). However, the evidence presented by this qualitative study of solvent-exchange kinetics suggests that IFN- $\alpha$ 2 binding induces considerable tightening and stabilization of the N-terminal FN-III domain in IFNAR2-EC. The change in the distribution of slowly exchanging amide protons is especially telling, with the vast majority of amide protons protected from exchange by IFN- $\alpha$ 2 binding located in the N-terminal subdomain containing the binding site. Notably, slowly exchanging amide protons in the N-terminal subdomain of the complex are distributed throughout the inner  $\beta$ -strands (S2, S3, and S6) and include but are not limited to residues involved in IFN- $\alpha$ 2 binding. Amide proton exchange is an indicator of the microstability of a polypeptide (55), and the change in solvent-exchange kinetics should therefore be attributed to a general "tightening" of the immunoglobulin scaffold, rather than to an extension of the  $\beta$ -strands or formation of intermolecular hydrogen bonds. Analysis of secondary chemical shifts of  $^{13}\text{C}_\alpha$  and  $^{13}\text{C}_\beta$  nuclei in the N-terminal subdomain of the IFNAR2-EC-IFN- $\alpha$ 2 complex did not discover any change in the location or length of the  $\beta$ -strands, and significant changes in chemical shifts were seen only for residues involved in IFN- $\alpha$ 2 binding. In addition, the intensity of inter- $\beta$ -strand NOE contacts observed for free IFNAR2-EC was weaker than expected, further supporting this hypothesis. These results are consistent with a previous study describing changes in amide proton exchange for an Fv fragment of an antibody induced by antigen binding. Solvent exchange rates along the Fv fragment were closely correlated to their proximity to the binding site, and protection from solvent exchange was propagated throughout the polypeptide, diminishing with increasing distance from the binding site (56). We conclude that it is a relatively flexible N-terminal domain that binds the incoming IFN- $\alpha$ 2, and the binding event leads to an increase in its rigidity.

The results of solvent-exchange experiments are intriguing when the structure of IFNAR2-EC in its biological context is considered. IFNAR2 is known to bind a multitude of IFN molecules, each initiating a distinct signaling cascade, and its versatility is a central question of IFN research (9). The observed flexibility may offer an explanation for this enigma.

The flexible N-terminal domain of IFNAR2 could adapt to meet the structural binding requirements of various ligands, thereby inducing specific structural changes in the receptor. The adaptable interdomain region may also contribute to this capability of the receptor. Even more interesting is the role that tightening of IFNAR2-EC may play in propagation of the IFN signaling cascade. IFNs trigger the signaling pathway by inducing the association of the two subunits of the IFNAR system, leading to cross-phosphorylation of kinases that are initially bound to the intracellular domains of both receptor components. The IFN-induced ternary receptor complex must therefore adopt a spatially well-defined conformation, if these preassociated kinases are to be correctly oriented for cross-activation. The increase in receptor rigidity may fix the receptor intracellular domains and kinases in the desired conformation and lead to phosphorylation, whereas such a productive encounter would have been unlikely for a more mobile receptor. Particularly significant is the involvement of the interdomain hinge region in IFN binding. A structural change in this segment induced by ligand binding would have a large effect on the interdomain angle and domain orientation, and could effectively lock IFNAR2 in the conformation necessary for further propagation of the IFN signal. The different binding sites for various IFN ligands upon the receptor may also modulate the observed tightening effect, accounting for their specific signaling pathways. The possible biological implications of the results of this study once again underline their relevance to the characterization of the function of IFN ligands and the receptor in this important biological system.

## ACKNOWLEDGMENT

We thank Dr. Jacob Piehler for IFNAR2-EC expression protocols and assistance with protein purification and Drs. Vitali Tugarinov and Tali Scherf for assistance with NMR experiments. We also acknowledge Dr. Miri Eisenstein for her guidance throughout the modeling process.

## SUPPORTING INFORMATION AVAILABLE

List of chemical shift assignments for free IFNAR2-EC. This material is available free of charge via the Internet at <http://pubs.acs.org>.

## REFERENCES

- Langer, J. A., and Pestka, S. (1985) *Pharmacol. Ther.* 27, 371–401.
- Stark, G. R., Kerr, I. M., Williams, B. R., Silverman, R. H., and Schreiber, R. D. (1998) *Annu. Rev. Biochem.* 67, 227–264.
- Weissmann, C., and Weber, H. (1986) *Prog. Nucleic Acid Res. Mol. Biol.* 33, 251–300.
- Pestka, S., Langer, J. A., Zoon, K. C., and Samuel, C. E. (1987) *Annu. Rev. Biochem.* 56, 727–777.
- Uze, G., Lutfalla, G., and Gresser, I. (1990) *Cell* 60, 225–234.
- Novick, D., Cohen, B., and Rubinstein, M. (1994) *Cell* 77, 391–400.
- Cohen, B., Novick, D., Barak, S., and Rubinstein, M. (1995) *Mol. Cell. Biol.* 15, 4208–4214.
- Platanias, L. C., and Fish, E. N. (1999) *Exp. Hematol.* 27, 1583–1592.
- Mogensen, K. E., Lewerenz, M., Reboul, J., Lutfalla, G., and Uze, G. (1999) *J. Interferon Cytokine Res.* 19, 1069–1098.
- Lewerenz, M., Mogensen, K. E., and Uze, G. (1998) *J. Mol. Biol.* 282, 585–599.
- Piehler, J., and Schreiber, G. (1999) *J. Mol. Biol.* 294, 223–237.
- Chuntharapai, A., Gibbs, V., Lu, J., Ow, A., Marsters, S., Ashkenazi, A., De Vos, A., and Jin Kim, K. (1999) *J. Immunol.* 163, 766–773.
- Runkel, L., deDios, C., Karpusas, M., Betzenhauser, M., Muldowney, C., Zafari, M., Benjamin, C. D., Miller, S., Hochman, P. S., and Whitty, A. (2000) *Biochemistry* 39, 2538–2551.
- Klaus, W., Gsell, B., Labhardt, A. M., Wipf, B., and Senn, H. (1997) *J. Mol. Biol.* 274, 661–675.
- Radhakrishnan, R., Walter, L. J., Hruza, A., Reichert, P., Trotta, P. P., Nagabhushan, T. L., and Walter, M. R. (1996) *Structure* 4, 1453–1463.
- Senda, T., Saitoh, S., and Mitsui, Y. (1995) *J. Mol. Biol.* 253, 187–207.
- Karpusas, M., Whitty, A., Runkel, L., and Hochman, P. (1998) *Cell. Mol. Life Sci.* 54, 1203–1216.
- Bazan, J. F. (1990) *Proc. Natl. Acad. Sci. U.S.A.* 87, 6934–6938.
- Walter, M. R., Windsor, W. T., Nagabhushan, T. L., Lundell, D. J., Lunn, C. A., Zauodny, P. J., and Narula, S. K. (1995) *Nature* 376, 230–235.
- Harlos, K., Martin, D. M., O'Brien, D. P., Jones, E. Y., Stuart, D. I., Polikarpov, I., Miller, A., Tuddenham, E. G., and Boys, C. W. (1994) *Nature* 370, 662–666.
- Uze, G., Lutfalla, G., and Mogensen, K. E. (1995) *J. Interferon Cytokine Res.* 15, 3–26.
- Piehler, J., and Schreiber, G. (1999) *J. Mol. Biol.* 289, 57–67.
- Seto, M. H., Harkins, R. N., Adler, M., Whitlow, M., Church, W. B., and Croze, E. (1995) *Protein Sci.* 4, 655–670.
- Ruf, W., Schullek, J. R., Stone, M. J., and Edgington, T. S. (1994) *Biochemistry* 33, 1565–1572.
- Neidig, K.-P., Geyer, M., Gorler, A., Antz, C., Saffrich, R., Beneicke, W., and Kalbitzer, H. (1995) *J. Biomol. NMR* 6, 255–270.
- Delaglio, F., Grzesiek, S., Vuister, G. W., Zhu, G., Pfeifer, J., and Bax, A. (1995) *J. Biomol. NMR* 6, 277–293.
- Grzesiek, S., and Bax, A. (1992) *J. Magn. Reson.* 96, 432–440.
- Ikura, M., Kay, L. E., and Bax, A. (1990) *Biochemistry* 29, 4659–4667.
- Grzesiek, S., and Bax, A. (1992) *J. Am. Chem. Soc.* 114, 6291–6293.
- Wittekind, M., and Mueller, L. (1993) *J. Magn. Reson., Ser. B* 101, 201–205.
- Grzesiek, S., Anglister, J., and Bax, A. (1993) *J. Magn. Reson., Ser. B* 101, 114–119.
- Grzesiek, S., and Bax, A. (1993) *J. Biomol. NMR* 3, 185–204.
- Marion, D., Driscoll, P. C., Kay, L. E., Wingfield, P. T., Bax, A., Gronenborn, A. M., and Clore, G. M. (1989) *Biochemistry* 28, 6150–6156.
- Clore, G. M., Kay, L. E., Bax, A., and Gronenborn, A. M. (1991) *Biochemistry* 30, 12–18.
- Kay, L. E., Clore, G. M., Bax, A., and Gronenborn, A. M. (1990) *Science* 249, 411–414.
- Vuister, G. W., and Bax, A. (1993) *J. Am. Chem. Soc.* 115, 7772–7777.
- Pervushin, K., Riek, R., Wider, G., and Wuthrich, K. (1997) *Proc. Natl. Acad. Sci. U.S.A.* 94, 12366–12371.
- Grzesiek, S., and Bax, A. (1993) *J. Am. Chem. Soc.* 115, 12593–12594.
- Grzesiek, S., Bax, A., Hu, J. S., Kaufman, J., Palmer, I., Stahl, S. J., Tjandra, N., and Wingfield, P. T. (1997) *Protein Sci.* 6, 1248–1263.
- Piotto, M., Saudek, V., and Sklenar, V. (1992) *J. Biomol. NMR* 2, 661–665.
- Sklenar, V., Piotto, M., Leppik, R., and Saudek, V. (1993) *J. Magn. Reson., Ser. A* 102, 241–245.

42. Rucker, S. P., and Shaka, A. J. (1989) *Mol. Phys.* 68, 509–517.
43. Shaka, A. J., Keeler, J., and Freeman, R. (1983) *J. Magn. Reson.* 53, 313–340.
44. Shaka, A. J., Barker, P. B., and Freeman, R. (1985) *J. Magn. Reson.* 64, 547–552.
45. Marion, D., and Wuthrich, K. (1983) *Biochem. Biophys. Res. Commun.* 113, 967–974.
46. Cavanagh, J., and Rance, M. (1990) *J. Magn. Reson.* 88, 72–85.
47. Bax, A., and Subramanian, J. (1986) *J. Magn. Reson.* 67, 565–570.
48. Salzmann, M., Wider, G., Pervushin, K., Senn, H., and Wuthrich, K. (1999) *J. Am. Chem. Soc.* 121, 844–848.
49. Spera, S., and Bax, A. (1991) *J. Am. Chem. Soc.* 113, 5490–5492.
50. Wuthrich, K. (1986) *NMR of proteins and nucleic acids*, John Wiley, New York.
51. Bork, P., Holm, L., and Sander, C. (1994) *J. Mol. Biol.* 242, 309–320.
52. Wilmot, C. M., and Thornton, J. M. (1988) *J. Mol. Biol.* 203, 221–232.
53. Hajduk, P. J., Meadows, R. P., and Fesik, S. W. (1999) *Q. Rev. Biophys.* 32, 211–240.
54. Anglister, J., Ren, H., Klee, C. B., and Bax, A. (1995) *FEBS Lett.* 375, 108–112.
55. Privalov, P. L., and Tsalkova, T. N. (1979) *Nature* 280, 693–696.
56. Williams, D. C., Jr., Rule, G. S., Poljak, R. J., and Benjamin, D. C. (1997) *J. Mol. Biol.* 270, 751–762.

BI011778F